Supporting Information

Artificial Intelligence-Integrated Overcoupled Resonator for Multifunctional Pesticide Spectral Classification and Quantification

Dongxiao Li[1,2,†], Ziwei Chen[3,†], Xueyuan Wu[3], Tao Liu[3], Guozhi Zhang[4], Xiaojing Mu[3,], and Chengkuo Lee[1,2,*]*

[1]Department of Electrical and Computer Engineering, National University of Singapore, 117583, Singapore

[2]Center for Intelligent Sensors and MEMS, National University of Singapore, 117608, Singapore

[3]Key Laboratory of Optoelectronic Technology & Systems of Ministry of Education, Chongqing University, Chongqing 400044, China

[4]Department of Electrical and Electronic Engineering, Hubei University of Technology, Wuhan 430068, China

[†] These authors contributed equally to this work.

* E-mail: (X. M.) mxjacj@cqu.edu.cn; (C. L.) elelc@nus.edu.sg

S1. Temporal coupled model theory

To better understand the role of plasmonic resonators in enhancing molecular vibrations, we established a simplified model based on the temporal coupled mode theory (TCMT). In this model, a metal–insulator–metal (MIM) structure is selected as the analytical platform due to its strong light–plasmon coupling capability and its suitability for achieving the overcoupled (OC) regime. The dynamic behavior of the MIM–molecule hybrid system is governed by the following TCMT equations:

$$\frac{d}{dt}P = j\omega_0 P - (\gamma_r + \gamma_a)P + \kappa S_{1+} + j\mu M \tag{S1}$$

$$\frac{d}{dt}M = j\omega_m M - \gamma_m M + j\mu P \tag{S2}$$

$$S_{1-} = -S_{1+} + \kappa P \tag{S3}$$

Here, P and M represent the modal amplitudes of the metamaterial resonator and molecular vibration, respectively. ω_0 and ω_m are the resonance frequencies of the resonator and molecule. γ_r and γ_a denote the radiative and absorptive losses of the resonator, while γ_m is the molecular absorption rate. κ is the coupling coefficient between the incident light and the resonator ($\kappa = (2\gamma_r)^{1/2}$), and μ describes the coupling strength between the resonator and the molecule. S_{1+} and S_{1-} are the incident and reflect wave amplitudes.

Since the MIM has a metallic ground plane, the transmission is zero (T=0), and the reflection $R=|r|^2$, while $r= S_{1+}/S_{1-}$. Therefore, absorption A=1-R becomes the key observable for surface-enhanced infrared absorption (SEIRA) spectroscopy analysis.

When molecules are introduced, the total absorption of the system is:

$$A=1-\left|\frac{2\gamma_r}{j(\omega-\omega_0)+(\gamma_r+\gamma_a)+\left(\frac{\mu^2}{j(\omega-\omega_m)+\gamma_m}\right)}-1\right|^2 \tag{S4}$$

For comparison, the absorption spectrum without molecules is given by:

$$A\big|_{\mu=0}=1-\left|\frac{2\gamma_r}{j(\omega-\omega_0)+(\gamma_r+\gamma_a)}-1\right|^2 \tag{S5}$$

The SEIRA enhancement spectrum can thus be expressed as the differential absorption:

$$\Delta A = A\big|_{\mu\neq 0} - A\big|_{\mu=0} \tag{S6}$$

To quantitatively assess the enhancement at the molecular resonance frequency $\omega=\omega_m$, we define the SEIRA sensitivity as:

$$I_{SEIRA} = \Delta A(\omega_m) \tag{S7}$$

Equation (S7) provides a method to quantify the extent to which molecular vibrations are enhanced by the resonator. To generalize the impact of different system parameters on molecular signal enhancement, we define the spectral detuning as $\Delta\omega=\omega_0-\omega_m$, representing the frequency offset between the resonator and the molecular vibration. Additionally, we define the loss ratio as $f=\gamma_r/\gamma_a$, which describes the relative contributions of radiative and absorptive losses within the resonator. To intuitively illustrate their effects, we fix the parameters as ω_m=1200 cm^{-1}, γ_a=20 cm^{-1}, μ=8 cm^{-1} and γ_m=8 cm^{-1}. By sweeping the values of ω_0 and γ_r, a two-dimensional sensitivity map can be generated, as shown in Figure 2c. This modeling framework provides theoretical guidance for designing resonators that optimize both vibrational signal enhancement and spectral bandwidth contrast.

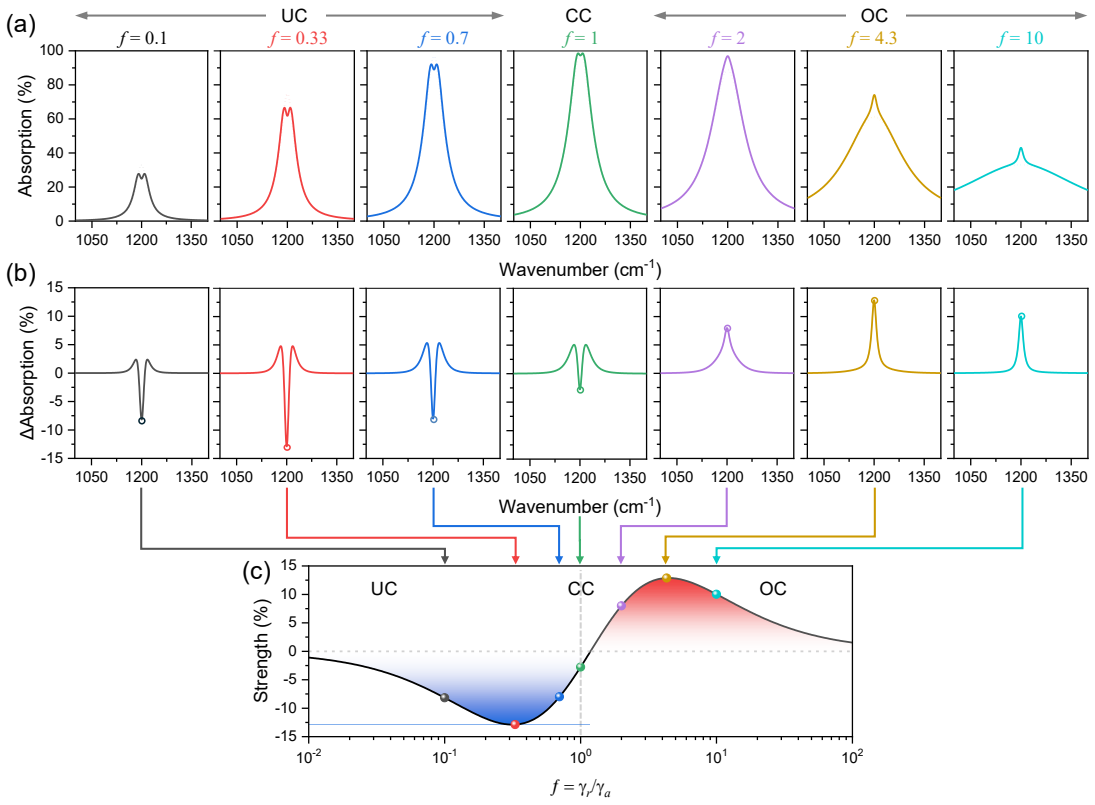

Figure S1. (a) Calculated absorption spectra of the MIM resonator before (dashed curves) and after (solid curves) coupling with molecules. The corresponding coupling factors are f = 0.1, 0.33, 0.7, 1, 2, and 10. (b) Absorption difference spectra extracted from (a). (c) MIM sensitivity as a function of the coupling factor f under spectral matching conditions ($\omega_m=\omega_0$). Here, we set $\omega_m=\omega_0$=1200 cm^{-1}, γ_a=20 cm^{-1}, μ=8 cm^{-1}, γ_m=8 cm^{-1}.

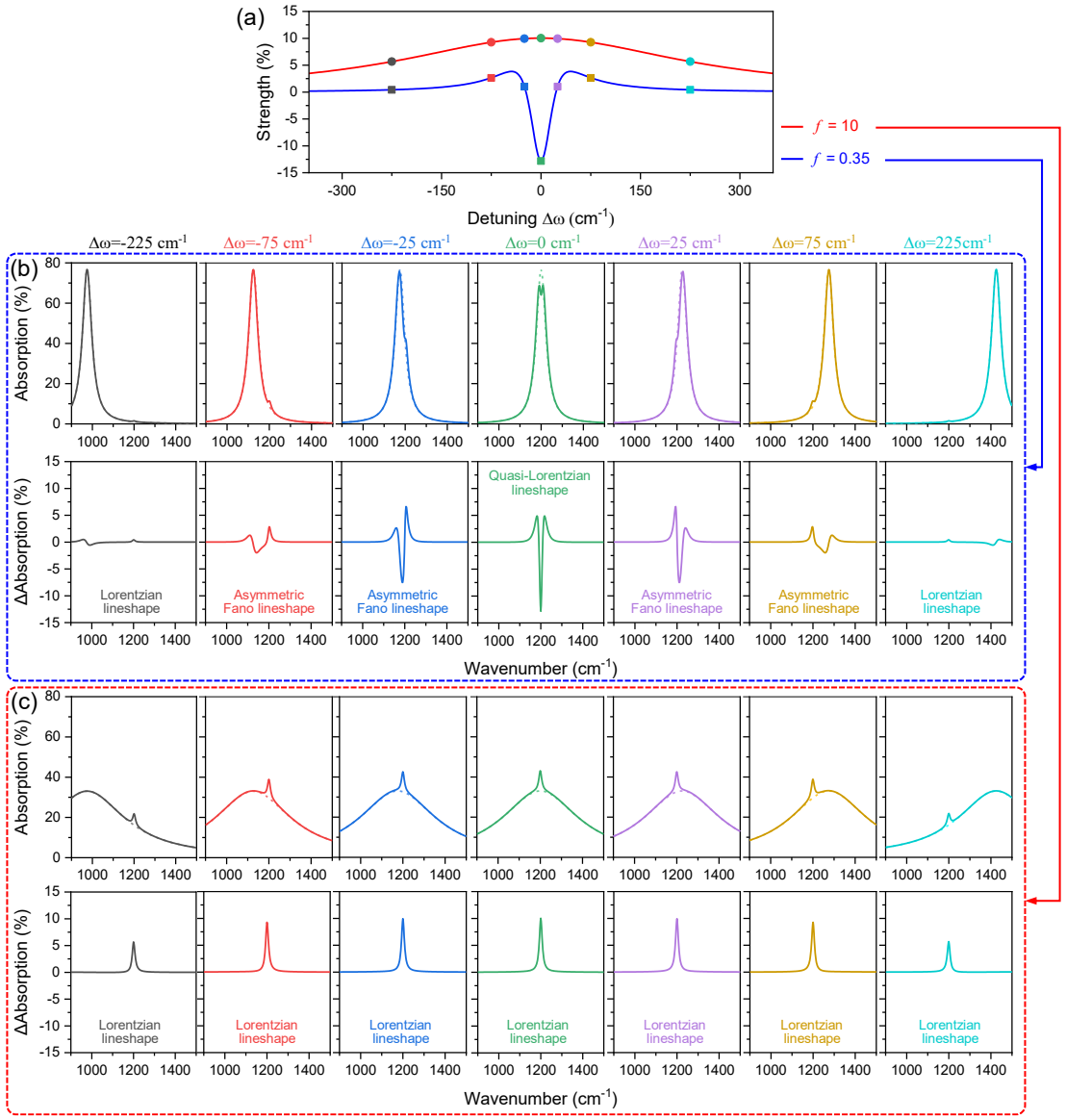

Figure S2. (a) Theoretically calculated sensitivity as a function of spectral detuning a f=0.35 (blue) and f=0.10 (red). Here, we set $\omega_m=\omega_0$=1200 cm^{-1}, γ_a=20 cm^{-1}, μ=8 cm^{-1}, γ_m=8 cm^{-1}. (b) Calculated absorption spectra of the MIM resonator before (dashed lines) and after (solid lines) coupling with molecules at f=0.35. The corresponding spectral detuning ($\Delta\omega$) are -225 cm^{-1}, -75 cm^{-1}, -25 cm^{-1}, 0 cm^{-1}, 25 cm^{-1}, 75 cm^{-1}, 225 cm^{-1}. (c) Absorption difference spectra calculated from panel (b). (d) Calculated absorption spectra of the MIM resonator before (dashed lines) and after (solid lines) coupling with molecules at f=10. The corresponding spectral detuning ($\Delta\omega$) are -225 cm^{-1}, -75 cm^{-1}, -25 cm^{-1}, 0 cm^{-1}, 25 cm^{-1}, 75 cm^{-1}, 225 cm^{-1}. (e) Absorption difference spectra calculated from panel (d).

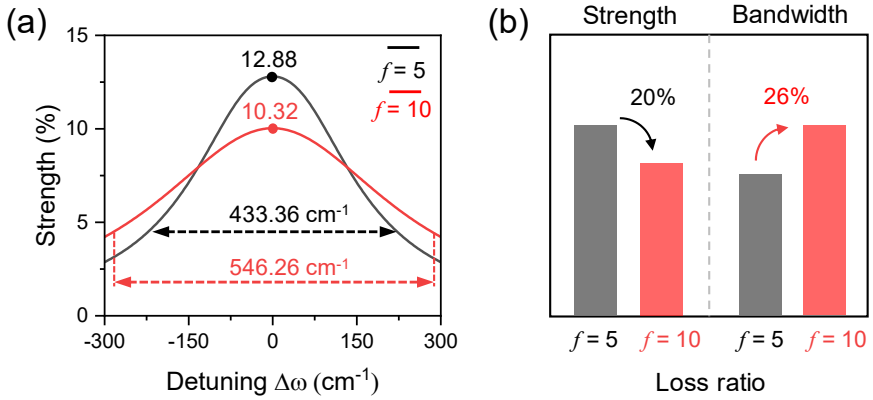

Figure S3. (a) Sensitivity as a function of spectral detuning under f=5 (black) and f=10 (red). (b) Bar chart comparing sensitivity and spectral bandwidth. Based on Equation S7 and the parameter settings of ω_m=1200 cm^{-1}, γ_a=20 cm^{-1}, μ=8 cm^{-1} and γ_m=8 cm^{-1}, the maximum I_{SEIRA} value is calculated to be 12.88%. Here, we define the spectral response bandwidth as the detuning range over which the sensitivity drops to 1/e of its maximum value (12.88%/e≈4.74%). According to this definition, when the loss ratio f = 5, the corresponding bandwidth is 433.36 cm^{-1}. When f = 10, the bandwidth increases to 546.26 cm^{-1}, representing an approximate enhancement of 26% compared to the f = 5 case ((546.26-433.36)/433.36≈26%). In addition, the maximum I_{SEIRA} value drops to 10.32% at f = 10, indicating a decrease of about 20% relative to the 12.88% achieved at f = 5 ((12.88%-10.32%)/12.88%≈20%).

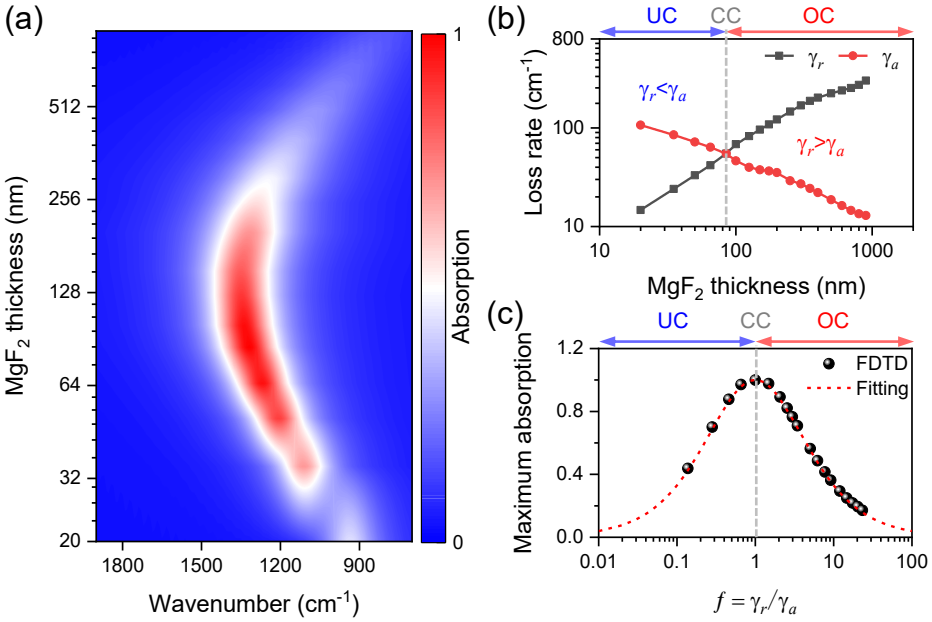

Figure S4. (a) Simulated absorption spectra as a function of the dielectric layer thickness. The schematic of the unit cell is shown in Figure 2b. The unit cell has a period of P = 2.5 μm, and the square nanoantenna has a side length of L = 2 μm. The thickness of the dielectric layer varies from 20 nm to 900 nm. The vertical axis is plotted on a logarithmic scale with base 2. (b) The radiative loss (γ_r) and absorptive loss (γ_a) are extracted from (a) using Equation S5. Both the horizontal and vertical axes are plotted on a logarithmic scale with base 10. As the dielectric thickness increases, radiative loss gradually exceeds absorptive loss. Notably, when the dielectric layer thickness is less than 85 nm, $\gamma_r < \gamma_a$, and the device operates in an undercoupled (UC) regime; at a thickness of 85 nm, $\gamma_r = \gamma_a$, corresponding to critical coupled (CC); and when the thickness exceeds 85 nm, $\gamma_r > \gamma_a$, indicating an OC regime. (c) Extracted the absorption intensity as a function of the loss ratio f from (a). The dashed curve represents the theoretical fitting result.

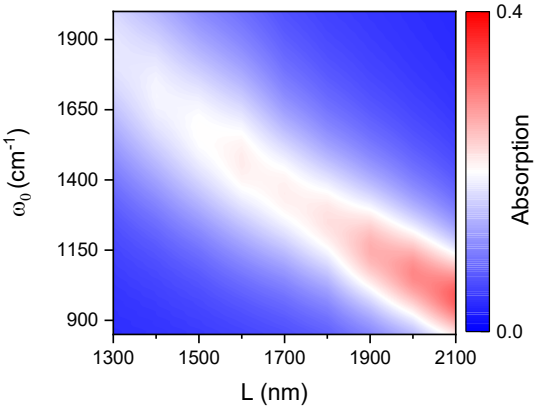

Figure S5. Simulated absorption spectra as a function of the square antenna side length (L). The schematic of the unit cell is shown in Figure 2a. The unit cell period is 2 μm, and the dielectric layer thickness is 500 nm. The side length L of the square antenna varies from 1.3 μm to 2.1 μm. As L increases, the resonance frequency gradually decreases.

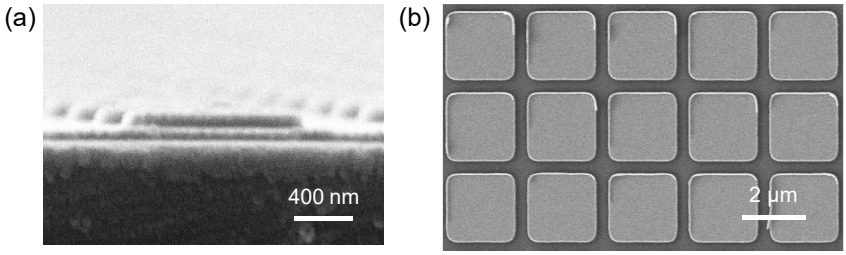

Figure S6. Scanning electron microscopy (SEM) images of UC resonator: a) cross-sectional view and b) top view. For the UC device, the dielectric layer thickness is 50 nm, the unit cell period is 2.5 μm, and the side length of the square antenna is 2.15 μm.

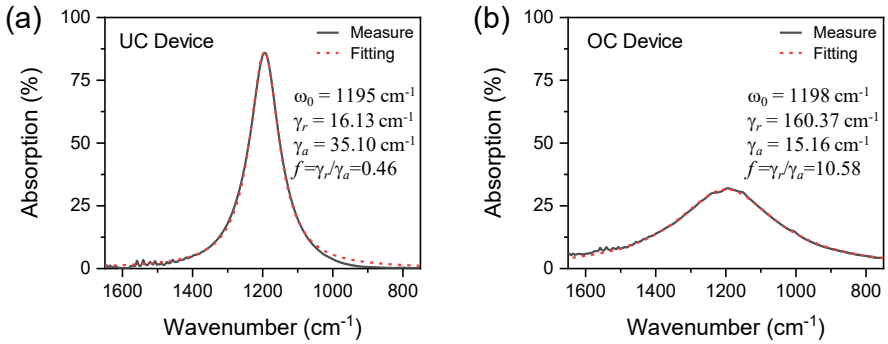

Figure S7. The black curves in (a) and (b) represent the measured spectra of the UC and OC devices, respectively. The red dashed curves are the fitted spectra based on Equation S5. The fitting results show that the fabricated UC device has a loss ratio f = 0.46, while the OC device exhibits a loss ratio of f = 10.58.

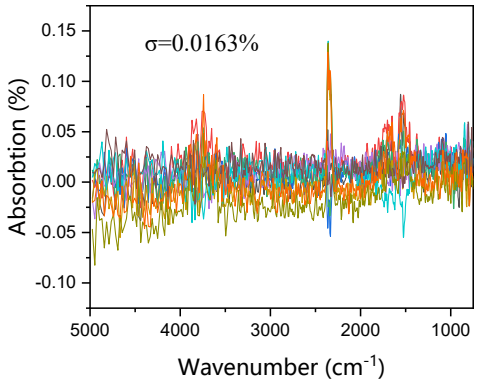

Figure S8. Fourier transform infrared spectroscopy (FTIR) measurements were repeatedly performed 10 times on a gold surface to evaluate the background noise. The average standard deviation of the noise was calculated to be 0.0163%.

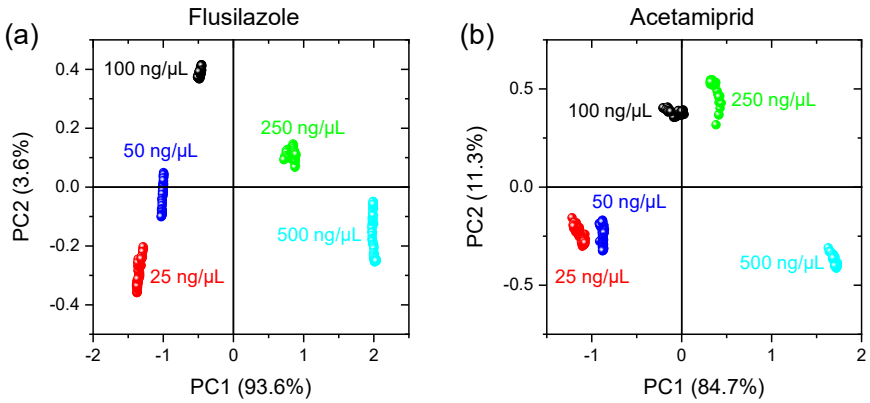

Figure S9. Principal component analysis (PCA) of flusilazole (a) and acetamiprid (b) at different concentrations. Each cluster represents a specific concentration.

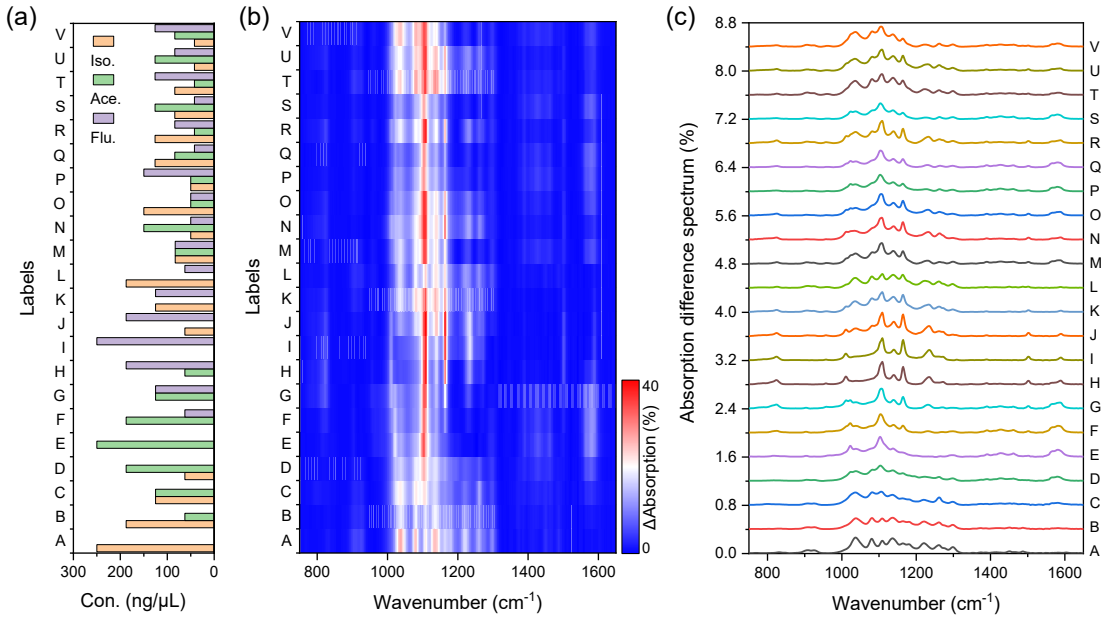

Figure S10. (a) Bar chart showing the titrated concentration combinations of three pesticide molecules. (b) SEIRA spectra extracted from Figure 4b. Each concentration combination includes 50 spectral measurements. (c) Representative SEIRA spectral curves extracted from (b), which contain information about different concentration ratios of the samples. However, due to the complexity of the pesticide fingerprint peaks and their spectral overlaps, manually distinguishing between concentration ratios is time-consuming and error prone. Therefore, we introduce artificial intelligence (AI) to analyze these spectral data.

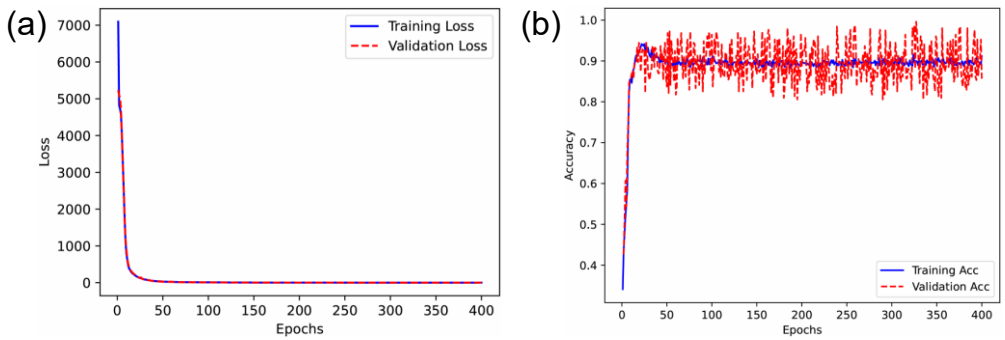

Figure S11. Multimodal deep neural network (MM-DNN) processing results in Figure 4f. (a) Loss of the MM-DNN model. (b) Accuracy of the MM-DNN model.

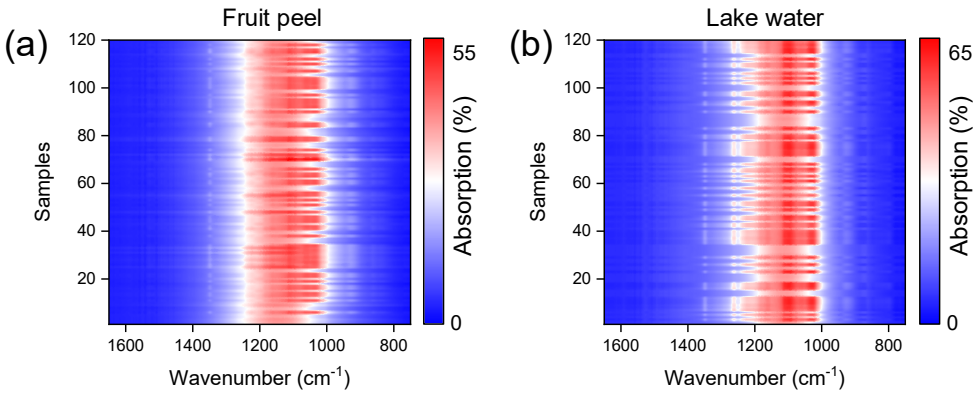

Figure S12. (a) Spectrum measurement of the presence or absence of pesticides on fruit peels. (b) Spectrum measurement of the presence or absence of pesticides in lake water.

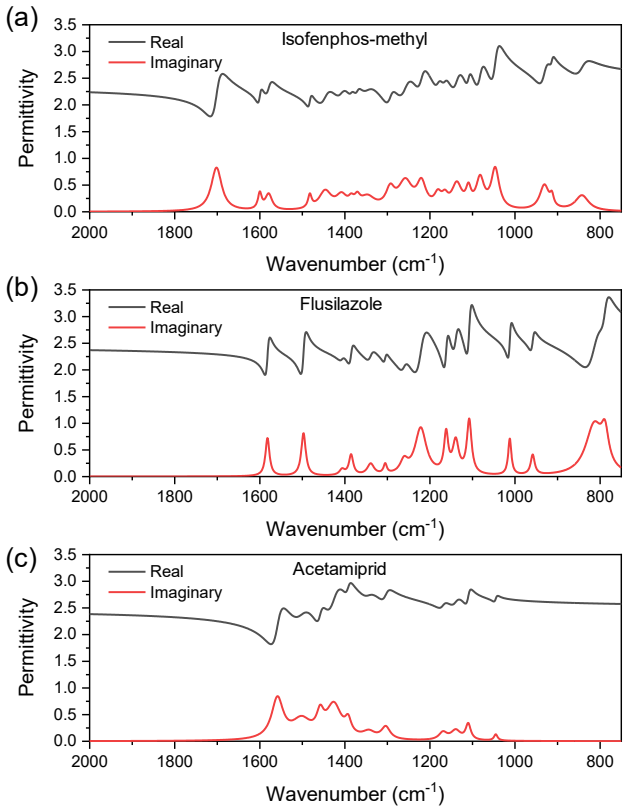

Figure S13. (a-c) Complex permittivity spectra of isofosmoticum-methyl (a), acetamiprid (b), and flusilazole (c). The black and red curves correspond to the real and imaginary parts of the complex permittivity, respectively. The complex permittivity function can be described by the Drude-Lorentz model, which is expressed as $\varepsilon(\omega) = \varepsilon_\infty + \sum_i \frac{\omega_{pi}^2}{\omega_{0i}^2 - \omega^2 - i\gamma_i\omega}$, where ε_∞ is the high-frequency dielectric constant. The parameters ω_{pi}, ω_{0i}, and γ_i represent the oscillator strength, intrinsic resonance frequency, and damping coefficient of the i-th Lorentz oscillator, respectively. The corresponding model parameters can be found in Tables S1-S3.

Table S1. Complex permittivity of isofenphos-methyl molecules (ε_∞=2.36). Units: cm^{-1}.

i	ω_{0i}	ω_{pi}	γ_i	*i*	ω_{0i}	ω_{pi}	γ_i
1	1701.77	204.67	30.07	12	1219.98	120.36	25.82
2	1599.87	71.46	10.63	13	1181.30	74.08	20.02
3	1579.05	96.27	19.49	14	1164.82	61.43	17.94
4	1482.23	61.51	10.39	15	1136.83	120.45	28.17
5	1446.45	133.05	35.50	16	1109.36	70.79	14.28
6	1407.88	101.70	30.64	17	1081.98	116.05	22.68
7	1384.89	51.47	15.32	18	1046.40	134.14	22.81
8	1370.70	58.80	15.69	19	930.96	107.55	26.51
9	1346.94	113.06	42.61	20	913.17	41.45	10.00
10	1293.29	103.11	24.55	21	842.64	96.63	38.11
11	1258.10	160.52	40.22				

Table S2. Complex permittivity of flusilazole molecules (ε_∞=2.44). Units: cm^{-1}.

i	ω_{0i}	ω_{pi}	γ_i	*i*	ω_{0i}	ω_{pi}	γ_i
1	1581.83	113.87	11.45	9	1161.81	99.92	11.74
2	1497.12	123.69	12.68	10	1139.27	109.47	17.39
3	1406.41	47.86	15.16	11	1107.56	121.52	13.20
4	1385.23	80.19	12.14	12	1012.18	79.21	9.12
5	1339.21	73.95	19.43	13	958.33	63.79	11.36
6	1305.07	47.64	9.54	14	813.94	193.98	49.15
7	1260.85	79.96	21.49	15	788.44	99.12	20.80
8	1221.64	187.57	32.57				

Table S3. Complex permittivity of acetamiprid molecules (ε_∞=2.46). Units: cm^{-1}.

i	ω_{0i}	ω_{pi}	γ_i	*i*	ω_{0i}	ω_{pi}	γ_i
1	1558.58	197.69	33.10	7	1303.78	86.14	24.66
2	1502.15	168.30	54.55	8	1169.31	61.84	23.07
3	1457.98	102.38	19.96	9	1139.37	75.41	27.40
4	1426.04	198.49	43.77	10	1109.93	68.77	14.27
5	1392.26	79.99	17.43	11	1045.00	35.19	10.11
6	1343.71	78.41	35.42				